

---

# Resolving Dark Pulses from Photon Pulses in NbN Superconducting Single-Photon Detectors

## Introduction

Fast and reliable single-photon detectors (SPD's) have become a highly sought after technology in recent years.<sup>1</sup> Some of the most interesting applications for SPD's, which include quantum communications and quantum key distribution,<sup>2</sup> as well as satellite communications, require devices that can successfully operate at telecommunication wavelengths, namely 1310 nm and 1550 nm. Another desirable feature for an ideal SPD is its photon-number resolution (PNR) capability.<sup>3,4</sup> InGaAs avalanche photodiodes work at telecommunication wavelength and are commercially available; they do, however, suffer from severe after-pulsing and require time gating, which limits their maximum count rate. Presently, they also lack the PNR capability.<sup>5,6</sup>

It has already been established that nanostructured, NbN superconducting single-photon detectors (SSPD's) operate based on hotspot formation and bias current redistribution in ultrathin (4 nm), narrow (100- to 120-nm), and long (~0.5-mm) meandering NbN superconductive stripes.<sup>1</sup> NbN SSPD's have been shown to have counting rates exceeding 250 MHz, with reported quantum efficiencies (QE's) up to 57% (Ref. 7) at 1550-nm wavelength and very low dark-count rates, ~10 Hz to 10 kHz, depending on the operation bias point.<sup>8</sup>

Typically, the SSPD's are kept at temperatures between 4.2 and 1.7 K (far below the NbN critical temperature  $T_c$ ), and biased at currents  $I_{\text{bias}}$  close to the meandering stripe critical current  $I_c$ . Once a photon is absorbed by the NbN nanostripe, it breaks a Cooper pair, and, subsequently, a large number of quasiparticles are generated through the electron–electron and electron–phonon interactions, creating a local hotspot where superconductivity is suppressed or even destroyed. The hotspot expels the supercurrent from its volume and forces it to flow near the stripe edges, where it can exceed the  $I_c$  value, leading to the generation of phase-slip centers and the eventual formation of a resistive region across the width of the stripe.

When the device is directly connected to a transmission line with the characteristic impedance  $Z_0$  equal to, e.g., 50  $\Omega$ ,

the above-mentioned resistive region, which is  $>50 \Omega$ , forces the bias current to redistribute from the SSPD into the load, which means that the amplitude of the SSPD voltage response is always simply the  $Z_0 I_{\text{bias}}$  product. The above conclusion is true even if the SSPD were illuminated by several photons and, consequently, several hotspots were simultaneously generated at various points along the meander. Thus, in the above typical experimental arrangement, the SSPD photoresponse is insensitive to the number and energy of incoming photons.

We need to stress that a biased SSPD can generate output electrical pulses even when the input light is completely blocked and there are no photons incident upon the device. The dark-count pulses are transient voltage signals, spontaneously generated in a current-biased, long, superconducting nanostripe, and their amplitude, when the device is connected to a 50- $\Omega$  line, is also close to  $Z_0 I_{\text{bias}}$ , despite the fact that their physical origin is different from the photon counts. In the case of dark counts, the transient resistive state across the SSPD stripe is, actually, due to the current-induced vortex–antivortex generation.<sup>9,10</sup>

The goal of this work is to show that, with our proposed new readout scheme, which implements a low-noise cryogenic amplifier and a high-load resistor next to the detector, we are able to resolve the difference between dark counts and photon counts in our devices. The same readout approach also leads to the photon-number–resolving and energy-resolving capabilities in our standard SSPD's,<sup>11</sup> making the SSPD a PNR-type and/or an energy-sensitive photon sensor.

## Device Description and Experimental Setup

SSPD's are patterned from epitaxial-quality NbN films, deposited by dc reactive magnetron sputtering onto sapphire substrates.<sup>12</sup> The films are characterized by a sheet resistance between 400 and 500  $\Omega/\text{sq}$  at room temperature, with  $T_c$  between 10 and 11 K, and the critical current density  $J_c \approx 10^6 \text{ A}/\text{cm}^2$ . The meander patterning is done by e-beam lithography and reactive ion etching. The films were deposited at the Moscow State Pedagogical University and patterned at Delft University of Technology. Perhaps because of the slight

differences in geometry, or slight patterning technique differences, the SSPD's in this work had three to four times lower  $I_c$ 's (~5 to 10  $\mu\text{A}$ ) than the typical Moscow fabricated and patterned devices.<sup>12</sup> The QE's, however, were on par with the standard  $10 \times 10\text{-}\mu\text{m}^2$  SSPD's, with the devices measured in this work having  $\text{QE} \approx 4\%$  at  $\lambda = 800\text{ nm}$ .

The standard SSPD operation setup is shown in Fig. 115.46(a). The device is wire bonded to a 50- $\Omega$  microstrip transmission line, coupled to a multimode optical fiber, and immersed into liquid helium.<sup>13</sup> The microstrip is then connected to a semirigid coaxial cable and at room temperature connected to a wideband bias-tee (0.08- to 26-GHz bandwidth). The bias-tee makes it possible to simultaneously amplify the transient photoresponse signal using a tandem of two broadband amplifiers (0.08- to 8.5-GHz bandwidth, 22-dB gain) and bias the SSPD by a stable low-noise dc voltage source. The amplified output signals, corresponding to photon counts and/or dark counts, are recorded by using either a Tektronix TDS 6604 digital single-shot (6-GHz-bandwidth) oscilloscope or a pulse counter. As a single-photon source, we use a tunable Ti:sapphire mode-locked laser, heavily attenuated. For dark-count measurements, the detector was blocked from all incoming radiation, i.e., shielded inside the dewar by a metallic enclosure.

An equivalent electrical model of the SSPD photoresponse is shown in Fig. 115.46(b). Kinetic inductance  $L_k$  is in series with a parallel arrangement of a hotspot resistance  $R_{\text{hs}}$  and a switch  $S$  represents the photodetection (switching) event in the SSPD. The detector is then connected to a dc bias source and a readout circuit, which consists in this case of a trans-

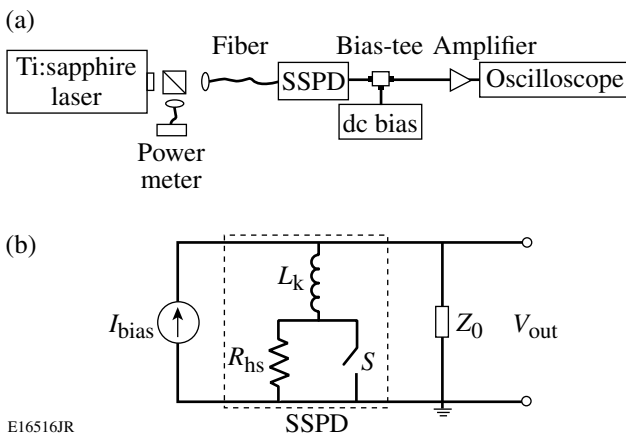


Figure 115.46  
(a) Experimental setup and (b) standard electrical photoresponse model of an SSPD.

mission line and amplifier with input impedance  $Z_0 = 50\ \Omega$ . In the simulations, which will be presented later, a bandpass filter representing the amplifier bandwidth is added. Finally,  $V_{\text{out}}$  is the experimentally observed transient voltage pulse during photodetection.

Initially, the switch is closed, and there is no voltage drop. Once a photon is absorbed by our nanostripe, the switch opens, and as  $R_{\text{hs}}$  grows to a value much larger than  $Z_0$ , most of the current redistributes into  $Z_0$ , and the resultant voltage pulse amplitude is simply  $V_{\text{out}} \approx GI_{\text{bias}}Z_0$ , where  $G$  is the amplifier gain. Thus, independent of the number or energy of the absorbed incident photons,  $V_{\text{out}}$  always has the same value for a given  $I_{\text{bias}}$  for the circuit shown in Fig. 115.46.

The new readout scheme presented here implements a high-electron-mobility transistor (HEMT) amplifier, operated cryogenically and mounted next to (on the same board) the SSPD. Because the HEMT input impedance is very high, a 500- $\Omega$  load (or shunt) resistor  $R_L$  is utilized in parallel with the detector and the HEMT, as shown in Fig. 115.47, which presents the circuit schematics. By applying the detector transient response to the gate of the HEMT, one can read out the amplified drain voltage, which should, ideally (for  $R_L \gg R_{\text{hs}}$ ), be proportional to the hotspot resistance and equal to  $V_{\text{out}} \approx GI_{\text{bias}}R_{\text{hs}}$ . If the number of photons simultaneously absorbed in the SSPD meander happens to be larger than 1, the photons are very likely to form separate hotspots and their resistances will add up in series. The HEMT output voltage in this case should be  $V_{\text{out}} \approx GI_{\text{bias}}nR_{\text{hs}}$ , where  $n$  is the number of absorbed photons per pulse (actually, the number of created hotspots).

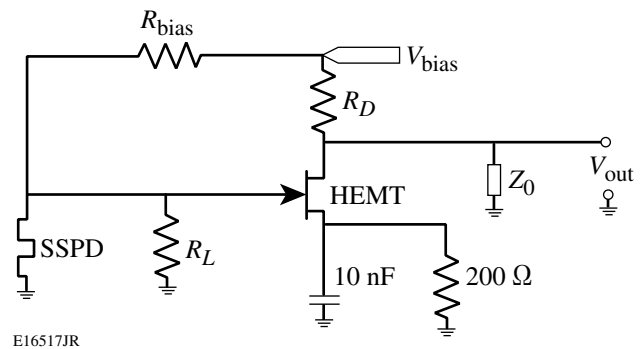


Figure 115.47  
Circuit schematics implementing a HEMT amplifier and a 500- $\Omega$  load resistor  $R_L$ . The 10-nF capacitor sets the maximum ac gain and the 200- $\Omega$  resistor sets the dc current for the HEMT;  $R_{\text{bias}}$  and  $R_D$  are the biasing and pull-up resistors, respectively.

Thus, for relatively small  $n$ 's, and  $nR_{\text{hs}} < R_L$ , the output pulse height of our setup is proportional to  $n$ , effectively leading to PNR.<sup>11</sup>

The HEMT setup should also enable one to distinguish pulses generated in response to either a single-photon absorption event (photon count) or a spontaneous voltage transient (dark count). In the case of dark counts, one can expect only a single localized resistive region, created due to the vortex-antivortex motion across the stripe, but its effective resistance should be different than  $R_{\text{hs}}$ , resulting in a somewhat different value of  $V_{\text{out}}$ .

Figure 115.48 compares photon-count time traces for the SSPD connected according to the standard scheme (Fig. 115.46) and the one with HEMT (Fig. 115.47). Even from this very short time trace, one can clearly see that with the standard-technique pulse amplitudes do not vary as much as those where the HEMT is utilized.

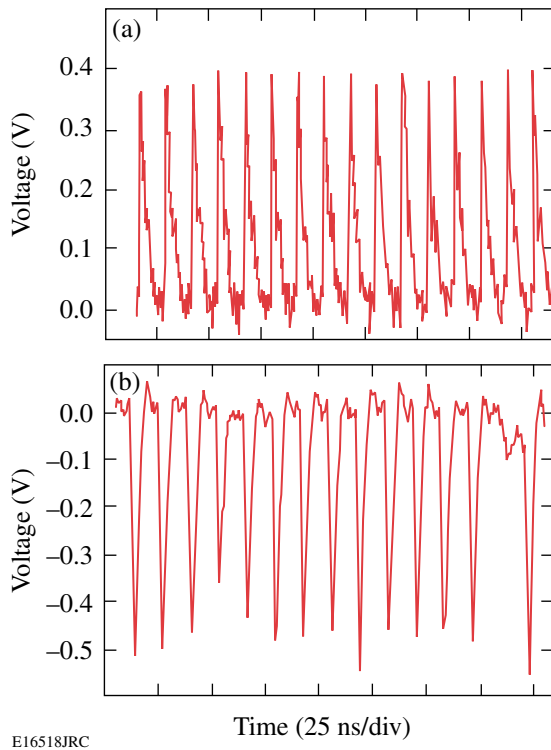


Figure 115.48 Comparison of real-time oscilloscope time-domain traces for (a) a traditional scheme (50- $\Omega$  load line) and (b) an HEMT readout scheme, taken at similar laser intensities, such that  $n \leq 1$  (HEMT is an inverting amplifier; therefore, the pulses are negative). The repetition rate of the laser was 82 MHz.

## Results and Discussion

In the experiments reported here, 700-nm-wavelength photons were used to compare time traces of photon events with dark-count events. Figure 115.49 shows histograms that compare pulse-amplitude distributions of the dark-count [Fig. 115.49(a)] and photon-count events [Figs. 115.49(b) and 115.49(c)] at two different laser intensities. All data were taken at the same bias current  $I_{\text{bias}} = 0.9 I_C$ .

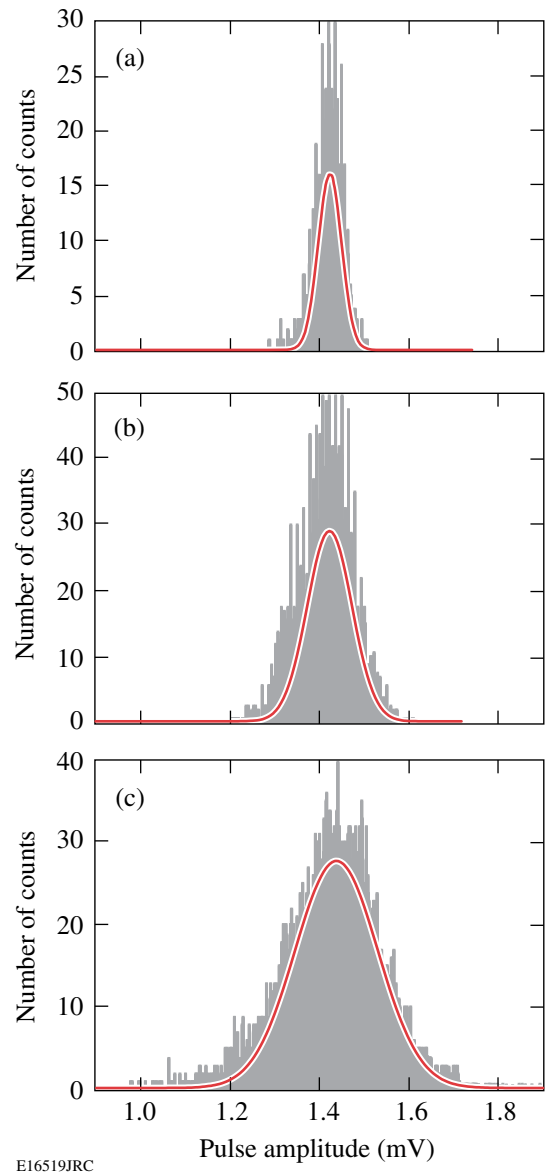


Figure 115.49 (a) Pulse-amplitude histograms of dark counts, (b) photon counts in the single-photon regime,  $n < 1$ , (c) and multiphoton regime,  $n \geq 1$ . All measurements performed at 4.2 K and at  $I_{\text{bias}} = 0.9 I_C$ . The SSPD output voltage amplitudes (x axis) are divided by the amplifier gain.

All histograms can be fit with a simple Gaussian function, and it is quite obvious from Fig. 115.49(a) that the dark counts have the narrowest distribution. It was shown previously<sup>10</sup> that, when the detector is blocked from all incoming radiation and placed in liquid helium shielded by a metallic enclosure, the spontaneous transient voltage pulses, or dark counts, are most likely due to topological excitations. The NbN film thickness of our devices is 4 nm, which puts the SSPD nanowire in a two-dimensional (2-D) superconductor regime because its thickness is smaller than the NbN Ginzburg–Landau coherence length. In 2-D systems in general, true long-range superconducting order is not possible, and in an ultrathin film, topological excitations come in the form of vortex–antivortex pairs (VAP’s).<sup>14</sup> VAP’s are superconducting analogous to electron-hole excitations in semiconductors.<sup>15</sup> At the typical SSPD operating temperature, and in the absence of  $I_{\text{bias}}$ , all VAP’s are bound and there is no dissipation in the NbN film. Once  $I_{\text{bias}}$  is applied, it exerts a Lorentz force on the VAP’s, and at  $I_{\text{bias}}$  close to  $I_c$ , this force is strong enough to exceed the VAP binding energy and break them. The latter effect creates free vortices (analog to excited carriers in semiconductors) and allows vortices and antivortices to move in opposite directions toward the edges of the NbN stripe, causing dissipation, and, in turn, the resistive state and Joule heating. The dark-counting rate in SSPD’s falls off quasi-exponentially with the biasing current.<sup>10</sup>

The photon-count amplitude distributions shown in Figs. 115.49(b) and 115.49(c), collected when the detector was irradiated by 700-nm photons, are clearly wider than that corresponding to the dark counts, even in the single-photon regime [Fig. 115.49(b)], when the average number of photons per pulse in the optical beam incident upon the

SSPD is  $n \ll 1$  (e.g., 0.01 photons per pulse). When the laser intensity was increased such that  $n \geq 1$ , we can see that the full width at half maximum (FWHM) of the distribution shown in Fig. 115.49(c) became over two times wider than that in Fig. 115.49(a).

The correlation between the beam intensity (average number of photons per pulse) incident upon the detector and the distribution FWHM of the response signals was very reproducible, and, as presented in Fig. 115.50, it depended on the SSPD bias current. One can clearly see that the dark-count signals (open squares) exhibit overall the narrowest distribution, which, in addition, is independent of the bias current.

For photon counts, the general trend is that the distribution width increases somewhat with increasing  $I_{\text{bias}}$ , and there is a wide jump between FWHM’s corresponding to the multiphoton ( $n \geq 1$ , closed triangles) and single-photon ( $n < 1$ , closed circles and open triangles) illumination. However, for  $n \ll 1$  (closed circles), as  $I_{\text{bias}}$  approaches  $I_c$ , the dark counts start to dominate over the photon counts and the amplitude distribution width starts to drop around  $I_{\text{bias}} = 0.83 I_c$ , eventually overlapping with open squares at  $I_{\text{bias}} > 0.9 I_c$ . The latter behavior agrees very well with our earlier observation that the rate of photon and dark counts depends on the  $I_{\text{bias}}/I_c$  ratio, as shown in the inset of Fig. 115.50.

When the laser intensity is set so that  $n \geq 1$  (closed triangles in Fig. 115.50), one can observe the widest distribution width of the SSPD response pulse. We believe that this behavior is related to the non-perfect fabrication of SSPD’s, resulting in some variations in the width or even the thickness of an NbN

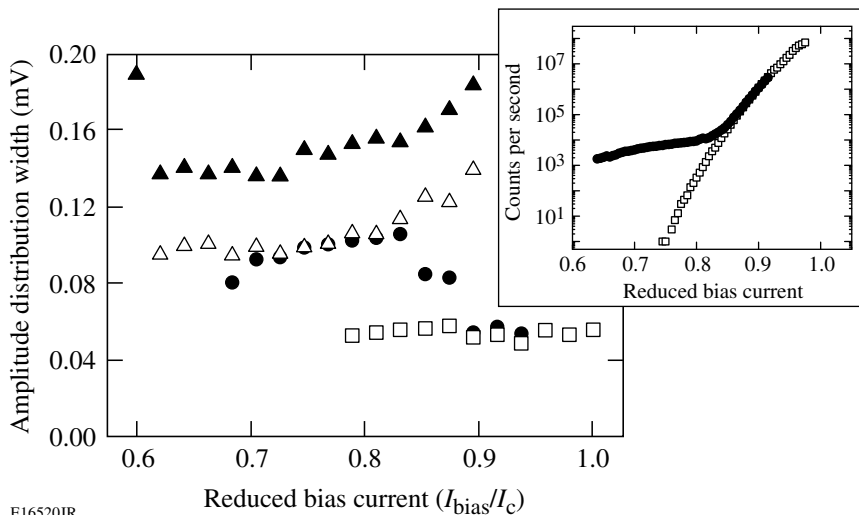


Figure 115.50  
Amplitude distribution width (FWHM of Gaussian fits) for dark counts (open squares),  $n < 1$  (closed circles),  $n \leq 1$  (open triangles), and  $n \geq 1$  (closed triangles). The inset shows the counting rate as a function of bias current for dark counts (open squares) and  $n < 1$  (closed circles).

meander stripe. Since the device  $I_c$  is determined by the narrowest and thinnest section(s) of the stripe, fluctuations in the stripe width must lead to variations of the final hotspot resistance, which in turn correspond to the broadened amplitude distributions of the photon-count responses. When light intensity is increased ( $n \geq 1$ ), more sections of the SSPD meander with, and apparently, different widths are activated, leading to enhanced fluctuations in the response pulse amplitudes and, finally, to the largest value of the distribution FWHM.

### Electrical Model and PSpice Simulations

If the electrical model only is considered, the difference in amplitude, for different hotspot resistances, stems from the time it takes for the current that initially biases the device to redistribute into the readout circuit. In other words, for a given  $R_L$ , current redistribution time decreases with increasing  $R_{hs}$ . For the hotspot to stop growing, and the cooling mechanism to take over, the current through the device must drop to a value below  $\sim 0.23 I_c$  (Ref. 16). When the SSPD photoresponse is modeled such that  $R_{hs}$  is a simple resistor, then the fall and rise time constants of the transient  $V_{out}$  are simply  $\tau_{fall} = L_k / (R_{hs} + R_L)$  and  $\tau_{rise} = L_k / R_L$  (Ref. 17), respectively. Unfortunately, this latter behavior is undesired if we want to observe PNR since, for a given  $R_L$ , the current redistribution time for two hotspots, which follows  $\tau_{fall} = L_k / (2R_{hs} + R_L)$  occurs faster than that for a single hotspot.

For PSpice modeling, the value of  $R_L$  was chosen to be 500  $\Omega$ , even though it was suspected that this value might be lower than the hotspot resistance. The reason is that higher  $R_L$  values can lead to an underdamped circuit because, as can be seen in Fig. 115.47, there is a large inductor ( $\sim 400$ -nH kinetic inductance of the SSPD) in parallel with  $R_L$ . In addition, in our readout circuit there is always a small parasitic capacitance estimated to be around 2 to 3 pF (coming from a circuit board, as well as other components). Figure 115.51(a) shows the PSpice simulated pulses for different values of  $R_L$ , and as can be seen, even for  $R_L = 500 \Omega$  (gray solid curve), the circuit is already slightly underdamped, as there is a small oscillation following the main pulse. Figure 115.51(b) shows the experimental (solid curve), as well as simulated (dashed curve), voltage pulses for our HEMT readout approach. The broader, more-damped oscillation behind the measured main pulse is likely due to some second-order effects from the amplifier and/or stainless steel coaxial line. Critical damping yielded  $R_L = 270 \Omega$  [dashed curve in Fig. 115.51(a)], which is actually a smaller value than the estimated hotspot resistance.

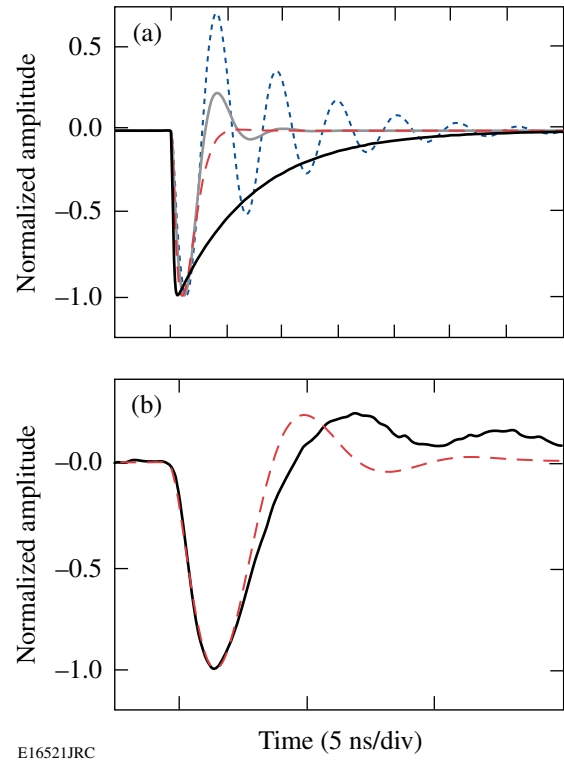


Figure 115.51  
(a) PSpice simulations of voltage transients at different values of  $R_L$ : 50  $\Omega$  (black solid curve), 270  $\Omega$  (dashed curve), 500  $\Omega$  (gray solid curve), and 2 k $\Omega$  (short-dashed curve); (b) measured photoresponse (solid curve) and simulated photoresponse (dashed curve), for  $R_L = 500 \Omega$ .

Finally, it must be mentioned that in order to fully model the behavior of an SSPD integrated with an HEMT readout, it is not enough to simply use the above electrical model, as there are many processes at play simultaneously. The Joule heating occurs in parallel with the cooling process and current redistribution,<sup>18</sup> so, ultimately, a more-complex physical model must be used, which is outside the scope of this work.

### Toward Photon-Number Resolution

As mentioned before and presented in Ref. 11, the integrated, cryogenic HEMT readout not only allows one to distinguish dark counts from photon counts, but it should also allow one to achieve PNR in SSPD's. For large  $R_L$ 's, the SSPD transient output pulse resulting from photodetection should be proportional in amplitude to the number of photons absorbed or, equivalently, the number of hotspots created in the SSPD. Unfortunately, it was shown by Ref. 18, in typical SSPD biased close to  $I_c$ , the  $R_{hs}$  can be as large as 5.5 k $\Omega$ , mainly due to Joule

heating. Even if it were possible to find a cryogenic amplifier with such large input  $R_L$ , the readout scheme would not work because the current would not be able to redistribute into the load fast enough before a runaway heating effect, and the device would simply latch.

Our devices, as mentioned before, have much lower than typical  $I_C$ 's, although they still operate quite well. With our  $I_{\text{bias}} \approx 5 \mu\text{A}$ , we estimate  $R_{\text{hs}}$  to be between 600 and 1000  $\Omega$ , so our selected  $R_L = 500 \Omega$  is reasonable and should make it possible, in principle, to distinguish between the single- and multiphoton events.

Indeed, when the laser intensity and  $I_{\text{bias}}$  were increased so that the detector started to register nearly every incident light pulse, while the dark counts were still low, we observed that, in time-domain traces, some response pulses exhibited visibly higher amplitudes than the rest. Figure 115.52 shows an example of such a time trace, which is quite convincing, but, of course, it is impossible to conclude that these large pulses were indeed due to double-photon events, instead of, e.g., a single-photon event arriving close in time to a dark-count event, or even resulting from inhomogeneities of our meander stripe and resulting longer current redistribution time. It was therefore very useful to look at the statistics of the pulse-amplitude distributions once again. This time, most of our measurements were done by varying the intensity of our laser pulses (mode-locked and twice up-converted light to get  $\lambda = 267 \text{ nm}$ ) and  $I_{\text{bias}}$ , and collecting amplitudes of several thousand pulses at each value of the laser intensity and  $I_{\text{bias}}$ .

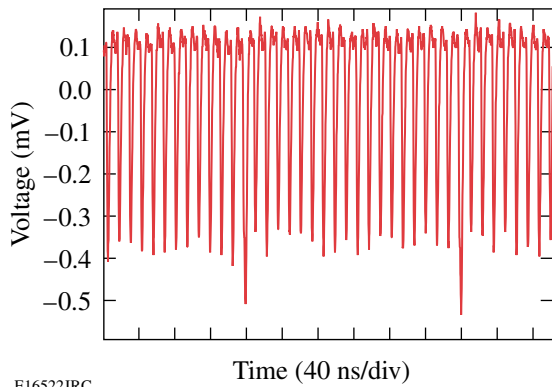


Figure 115.52  
Real-time oscilloscope trace-domain trace, showing higher pulse amplitudes of some pulses.

The results are presented in Fig. 115.53. When  $I_{\text{bias}} \approx 0.7 I_C$ , the amplitude distribution could be easily fit with a simple Gaussian function, as shown in Figs. 115.53(a) and 115.53(b). However, once  $I_{\text{bias}}$  reached  $0.9 I_C$ , as shown in Figs. 115.53(c) and 115.53(d), we started to see a clear second peak at lower amplitudes, and the distribution now had to be fit with two Gaussians. The latter can be easily explained by the varying width (nonuniformity) of the NbN stripe: at higher  $I_{\text{bias}}$ , more (wider) sections of the SSPD meander were activated for photodetection, giving rise to the second Gaussian peak. This peak is expected to be centered at lower amplitudes, because Joule heating in the wider sections should give rise to lower  $R_{\text{hs}}$ , as in those sections we should expect a better heat dissipation into the substrate than that in the narrower sections.

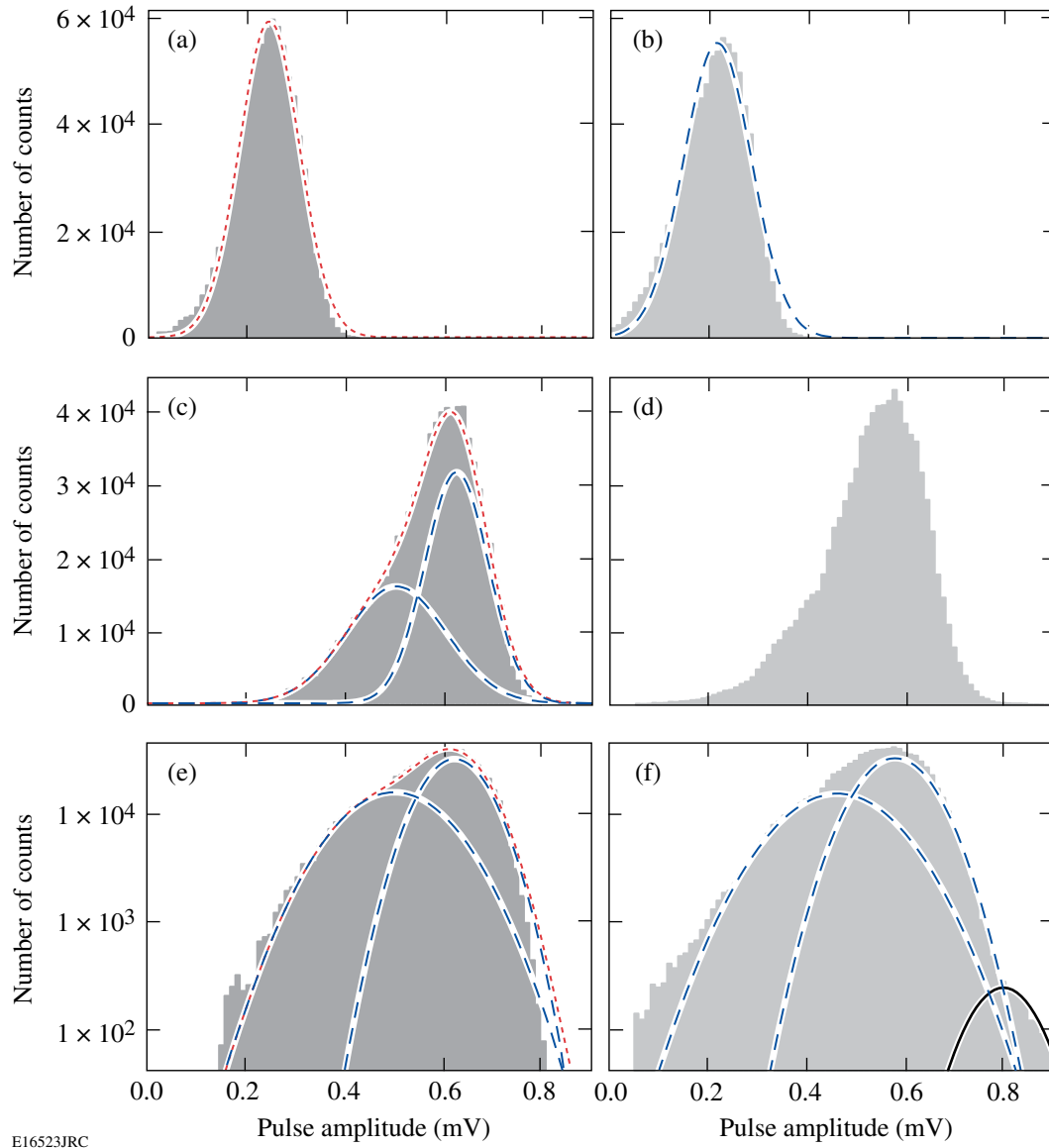
When the data shown in Figs. 115.53(c) and 115.53(d) were plotted on a semi-log scale, as presented in Figs. 115.53(e) and 115.53(f), respectively, it became quite clear that in the  $n \leq 1$  regime [Fig. 115.53(f)] there was, actually, a third small peak centered around 0.8 mV. This peak was completely absent in the  $n \ll 1$  regime [Fig. 115.53(e)] and when  $I_{\text{bias}}$  was below  $0.78 I_C$ . At present, we have no clear interpretation for the existence of this third peak. It cannot be related to the dark counts since they fall off exponentially with  $I_{\text{bias}}$  and are nearly zero below  $0.85 I_C$ . Thus, the most-reasonable, tentative explanation is that it is indeed due to the SSPD detection of multiphoton events. Further analysis and calculations are needed to either support or disprove this conclusion.

## Conclusion

We were able to resolve the difference between dark counts and photon counts in our NbN SSPD by utilizing an HEMT amplifier readout technique and examining pulse-amplitude distribution widths. The dark-count distribution width is very narrow for a given bias current, while that for photon counts is up to 2.5 times wider and is clearly related to the incident photon flux upon the SSPD (the average number of photons per pulse). The latter demonstrates that the HEMT readout is a promising approach in the future for PNR measurements.

## ACKNOWLEDGMENT

This work was supported in part by the U.S. AFOSR grant FA9550-06-1-0348 and the NYSTAR grant to the University of Rochester CAT-EIS. We would also like to thank Prof. G. Gol'tsman and his group at the Moscow State Pedagogical University for their assistance in sample preparation and Prof. H. Mooij for very helpful discussions.



E16523JRC

Figure 115.53

Pulse-amplitude histograms for (a)  $n < 1$ ,  $I_{\text{bias}} = 0.7 I_C$ , (b)  $n \leq 1$ ,  $I_{\text{bias}} = 0.7 I_C$ , (c)  $n < 1$ ,  $I_{\text{bias}} = 0.9 I_C$ , (d)  $n \leq 1$ ,  $I_{\text{bias}} = 0.9 I_C$ , (e) semi-log plot of (c), (f) semi-log plot of (d) (dark gray histograms indicate the same incident photon flux for the  $n < 1$  regime; light gray histograms indicate the same incident photon flux for the  $n \leq 1$  regime).

## REFERENCES

1. W. Słysz, M. Węgrzecki, J. Bar, P. Grabiec, M. Górska, V. Zwiller, C. Latta, P. Böhi, A. J. Pearlman, A. S. Cross, D. Pan, J. Kitaygorsky, I. Komissarov, A. Verevkin, I. Milostnaya, A. Korneev, O. Minayeva, G. Chulkova, K. Smirnov, B. Voronov, G. N. Gol'tsman, and R. Sobolewski, *J. Mod. Opt.* **54**, 315 (2007).
2. C. Bennett and G. Brassard, in *International Conference on Computers, Systems, and Signal Processing* (IEEE Computer Society, IEEE Circuits and Systems Society, and Indian Institute of Science, Bangalore, India, 1984), pp. 175–179.
3. E. Waks, A. Zeevi, and Y. Yamamoto, *Phys. Rev. A* **65**, 052310 (2002); G. Brassard *et al.*, *Phys. Rev. Lett.* **85**, 1330 (2000).
4. E. Knill, R. Laflamme, and G. J. Milburn, *Nature* **409**, 46 (2001).
5. Y. Kang *et al.*, *Appl. Phys. Lett.* **85**, 1668 (2004).
6. G. Ribordy *et al.*, *J. Mod. Opt.* **51**, 1381 (2004).
7. K. M. Rosfjord *et al.*, *Opt. Express* **14**, 527 (2006).

8. J. Kitaygorsky, J. Zhang, A. Verevkin, A. Sergeev, A. Korneev, V. Matvienko, P. Kouminov, K. Smirnov, B. Voronov, G. Gol'tsman, and R. Sobolewski, *IEEE Trans. Appl. Supercond.* **15**, 545 (2005).
9. A. Engel *et al.*, *Phys. Stat. Sol. C* **2**, 1668 (2005).
10. J. Kitaygorsky, I. Komissarov, A. Jukna, D. Pan, O. Minaeva, N. Kaurova, A. Divochiy, A. Korneev, M. Tarkhov, B. Voronov, I. Milostnaya, G. Gol'tsman, and R. Sobolewski, *IEEE Trans. Appl. Supercond.* **17**, 275 (2007).
11. M. G. Bell *et al.*, *IEEE Trans. Appl. Supercond.* **17**, 289 (2007).
12. G. N. Gol'tsman, K. Smirnov, P. Kouminov, B. Voronov, N. Kaurova, V. Drakinsky, J. Zhang, A. Verevkin, and R. Sobolewski, *IEEE Trans. Appl. Supercond.* **13**, 192 (2003).
13. W. Słysz, M. Węgrzecki, J. Bar, P. Grabiec, M. Górską, V. Zwiller, C. Latta, P. Böhi, I. Milostnaya, O. Minaeva, A. Antipov, O. Okunev, A. Korneev, K. Smirnov, B. Voronov, N. Kaurova, G. Gol'tsman, A. Pearlman, A. Cross, I. Komissarov, A. Verevkin, and R. Sobolewski, *Appl. Phys. Lett.* **88**, 261113 (2006).
14. J. E. Mooij, in *Percolation, Localization, and Superconductivity*, edited by A. M. Goldman and S. A. Wolf, NATO ASI, Series B, Vol. 109 (Plenum Press, New York, 1984), pp. 325–370.
15. A. M. Kadin, *J. Appl. Phys.* **68**, 5741 (1990).
16. A. VI. Gurevich and R. G. Mints, *Rev. Mod. Phys.* **59**, 941 (1987).
17. A. J. Kerman *et al.*, *Appl. Phys. Lett.* **88**, 111116 (2006).
18. J. K. W. Yang *IEEE Trans. Appl. Supercond.* **17**, 581 (2007).